Rock Mechanics and Rock Engineering
https://doi.org/10.1007/s00603-024-03974-8

ORIGINAL PAPER

Bentonite Swelling into Voids: Different Modelling Approaches for Hydration with Technological Gaps

Liliana Gramegna[1] · Gabriele Della Vecchia[1] · Robert Charlier[2]

Received: 23 December 2023 / Accepted: 8 May 2024

Abstract

Bentonite-based materials have emerged as a highly promising choice for engineered barriers in nuclear waste deep geological disposal. These materials are characterised by low permeability, high swelling capacity and effective radionuclide retardation, making them suitable for sealing underground galleries and canisters containing nuclear waste. However, the presence of technological gaps within the bentonite or the host rock can significantly influence their hydromechanical behaviour, potentially creating preferential pathways for radionuclide migration, thus affecting the overall performance of the engineered barrier. In this study, two different modelling strategies (namely, "gap" and "no-gap") to reproduce technological gaps and their effect on the hydromechanical behaviour of bentonite-based materials during intermediate saturation stages are proposed. The numerical model is used to simulate laboratory tests, and the numerical results are compared with experimental data coming from hydration test conducted under overall constant volume (isochoric) conditions. It is noteworthy that the specimen used in the experimental study is characterised by a localised gap between its side and the cell wall. The paper highlights the benefits of the "gap" numerical model, which employs interface elements to reproduce technological gaps at the side of the cell and exhibits satisfactory capabilities in reproducing the experimental swelling pressure evolution during bentonite hydration, especially during the transient wetting stages. Significant implications are expected for predicting site performance of engineered barrier systems in nuclear waste disposal applications.

Highlights

- The effect of technological gaps on the hydro-mechanical behaviour of bentonite-based materials for nuclear waste disposal is investigated.
- Two different modelling strategies, "gap" and "no-gap", are proposed to simulate the presence of technological gaps in the bentonite.
- The numerical results are compared with experimental data from a hydration test under constant volume conditions.
- The advantages of the "gap" numerical model, which can reproduce the experimental swelling pressure evolution more accurately, are demonstrated and its implications are discussed for the performance of engineered barrier systems.

Keywords Bentonite hydration · Technological gaps · Nuclear waste disposals · Finite element · Modelling

1 Introduction

Bentonite-based materials have been identified as one of the most reasonable choices for engineered barriers in the context of deep geological disposal of nuclear waste. These materials can be used to seal underground galleries and shafts, as in the French CIGEO concept (Labalette et al. 2013), but also placed in direct contact with canisters

✉ Liliana Gramegna
liliana.gramegna@polimi.it

[1] Department of Civil and Environmental Engineering, Politecnico di Milano, P.zza Leonardo da Vinci 32, 20133 Milan, Italy

[2] Département ArGEnCo - Géotechnique, Géomécanique et Géologie de l'Ingénieur, Université de Liège, 4000 Liège 1, Belgium

Published online: 05 June 2024

containing nuclear waste, as in the EB experiment (Alonso et al. 2010). The sealing capacity of these expansive clays is commonly related to their very low permeability in saturated conditions, high swelling ability and effective radionuclide retardation capacity (Cui 2017; Pusch 1979; Sellin and Leupin 2013). However, the efficiency of bentonite barriers can be severely compromised by the presence of unavoidable technological gaps within the bentonite itself or between the bentonite plug and the host rock (e.g. Mokni et al. 2016). These technological gaps are, for instance, the openings created during the construction of the repository, and can represent potential preferential pathways for water, gas and radionuclides migration (Villar et al. 2023). Moreover, both permeability and swelling pressure are related to dry density, which is expected to decrease upon swelling in technological voids. Technological gaps have been quantified at 6.6, 12 and 14% of the total volume of the galleries in the FEBEX mock-up test (Martin et al. 2006), PGZ2 in situ tests in the Underground Research Laboratory (URL) at Bure (Gatabin et al. 2016) and SEALEX in situ test (Wang et al. 2013; Saba et al. 2014), respectively.

However, during the early lifetime of the barrier, groundwater coming from the surrounding host rock progressively hydrates the bentonite, inducing its swelling and the filling up of these voids (Villar and Lloret 2008). As the gaps close and contact is formed, swelling pressure begins to develop under confined conditions. The initial free swelling followed by isochoric hydration can lead to an inhomogeneous distribution of the bentonite dry density and a subsequent reduction in the overall swelling pressure of the repository. This inhomogeneity can significantly influence the local bentonite hydraulic and mechanical properties, for instance creating preferential flow path for radionuclides, and potentially impacting the performance of the engineered barrier (Bian et al. 2019). Therefore, a thorough understanding of the behaviour of bentonite upon hydration under various constraints (e.g. free swelling or constant volume) is paramount to assess the long-term stability and performance of such sealing structures. Due to its relevance, numerous researchers have recently examined the impact of technological voids on the hydromechanical behaviour of bentonite, especially from an experimental point of view (e.g. Daniels et al. 2021; Harrington et al. 2020; Villar et al. 2023; Wang et al. 2021; Watanabe and Yokoyama 2021; Zeng et al. 2022, amongst others). However, numerical hydromechanical analyses are also of paramount importance, especially for the evaluation of the long-term behaviour of the barrier: nevertheless, the numerical hydromechanical analysis of the bentonite hydration process in the presence of voids still poses significant challenges. In this paper, two hydromechanical numerical models have been developed to reproduce the response of a bentonite sample upon hydration when a technological gap between the specimen side and the cell wall is present. In particular, the "gap" model considers the presence of the gap via the introduction of suitable interface elements, whilst the "no-gap" model neglects the presence of the technological gap. Although these assumptions in the numerical model have a significant impact on the evolution of the numerical predictions, to the authors' knowledge, they have not been thoroughly investigated. The hydromechanical numerical model is implemented in the numerical code LAGAMINE (Collin et al 2002), and takes advantage of the Barcelona Basic Model (BBM, Alonso et al. 1990) to reproduce the bentonite mechanical behaviour in unsaturated conditions. Despite some models specifically developed to reproduce the hydromechanical behaviour of expansive clay behaviour are available (see, e.g. Gens and Alonso 1992, Alonso et al. 1999, Musso et al. 2013, Della Vecchia and Musso 2016, Navarro et al. 2020), BBM is here preferred due to its simplicity, robustness, efficiency and limited number of material parameters. The influence of the interaction between intra- and inter-aggregate voids (often named micropores and macropores) for the compacted bentonite is explicitly considered just in terms of water retention behaviour and water permeability evolution, according to the double porosity model proposed in Della Vecchia et al (2015) and Dieudonné et al. (2017). The experimental activity has been developed in the framework of the BEACON project (Bentonite Mechanical Evolution): in this paper, an experimental test considering overall isochoric hydration conditions, but characterised by a technological gap between the specimen side and the cell wall, has been exploited. The test results, already cited in Bernachy-Barbe (2021) and Gramegna et al. (2022), are here enhanced with further experimental information, allowing a qualitative and quantitative evaluation of the performance of the two modelling approaches proposed.

Using both experimental data, including swelling pressure and suction measurements, and the results of numerical simulations, this work aims to highlight the relevance of different modelling assumptions in the context of compacted bentonite swelling for nuclear waste disposal applications. In particular, the combination of experiments and numerical analyses contributes to a comprehensive understanding of the consequences of modelling assumptions on the hydromechanical behaviour of bentonite-based materials during intermediate saturation phases when surrounded by technological gaps, which can contribute to a safer design of large-scale in situ structures.

2 Material and Experimental Testing Methodology

The test presented in this paper is part of an experimental campaign conducted to study the hydration process, specifically under isochoric conditions, of several bentonite

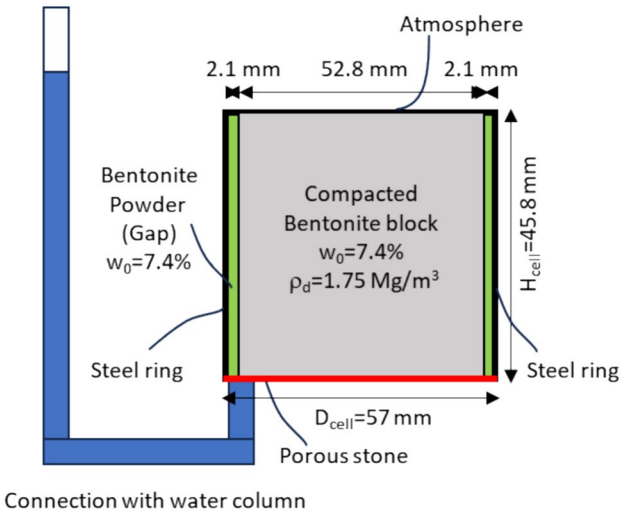

Fig. 1 Schematic of the experimental device

samples with similar overall dry density, but with different initial pore size distribution and hydration length (Bernachy-Barbe 2021). The bentonite material considered is Wyoming bentonite (MX-80 type) supplied by Laviosa MPC, which contains a significant amount of smectite (77%) along with minor inclusions of non-clay minerals such as micas (~ 1%), quartz (~ 8%), gypsum (~ 1%), calcite (~ 1%) and feldspars (~ 12%) (Tang et al. 2008; Guerra et al. 2017). The cation exchange capacity of the bentonite is equal to 98 meq/100 g (Saba et al. (2014), Guerra et al. (2017)). The experiments were conducted with the aim of identifying the role of initial heterogeneous dry density distribution on the development of swelling pressure upon wetting (Baryla et al. 2019).

In particular, the test C_6 (as named in Bernachy-Barbe (2021) and Gramegna et al. (2022), Fig. 1) of the BEACON project is here considered. A MX-80 bentonite block was compacted in isotropic conditions at an initial dry density of ρ_d = 1.75 Mg/m^3 and an initial water content of w = 7.44%. To achieve isotropic compaction, the clay, first placed in a neoprene tube (diameter 90 mm, length 120 mm, thickness 1.2 mm), underwent compression in an isotropic cell up to an all-around stress of 40 MPa, until the achievement of the target dry density of ρ_d = 1.75 Mg/m^3. The specimen was then removed from the isotropic cell and shaped to fit into another cell, called in the following 'equipped cell'. After shaping, the final block height was 45.82 mm and the final diameter was 52.8 mm (the diameter of the isotropic cell was 57 mm). Once placed in the equipped cell, the radial gap between the bentonite block and the side of the cell was filled with 3.35 g of loose bentonite powder (w = 7.44%). Bentonite powder indicates the bentonite material obtained by crushing large pellets at their hygroscopic water content, selecting only the grains passing through the 2-mm sieve, as in Bernachy-Barbe (2021). In particular, for the bentonite powder, a passing fraction of 60% corresponds to D_{60} = 1 mm, whilst a passing fraction of 10% corresponds to D_{10} = 0.06 mm. Being the volume of the gap 16.3 cm^3 and assuming a homogeneous powder distribution inside the gap, the average dry density of the powder can be estimated as 0.191 Mg/m^3. The target final average dry density of the sample (i.e. made of the block and the gap) in the cell, if assumed homogeneous, was $\rho_d \approx 1.52$Mg/m^3.

The reason for the introduction of loose powder in the gap is twofold: on the one hand, it is necessary to minimise the risk of instantaneous flooding of the injected water along the discontinuity between the block and the cell, which would undermine the results of the test; on the other hand, its very low dry density guarantees the development of negligible swelling pressure upon wetting, resembling the behaviour of a gap from the mechanical point of view. The initial suction of the bentonite and the powder is approximately equal to 100 MPa, as obtained by published water retention curve data (e.g. Villar 2004, see Table 1 in Sect. 3). The constant volume cell used in the experiments has been already described in Imbert and Villar (2006) and it is only briefly summarised herein. The device, a multi-sensor oedometric cell of 57 mm diameter and 47 mm height, was equipped with sensors at different heights, allowing the measurement of the radial total stress, the relative humidity and the temperature. In particular, the three relative humidity sensors were placed at three different heights (z = 6.6 mm, z = 23.3 mm and z = 40 mm from the bottom of the sample), whilst the nine total pressure sensors were placed at three heights (z = 6.6 mm, z = 23.3 mm and z = 40 mm from the bottom of the sample) and three angular positions (see Bernachy-Barbe (2021) for further details). A water column and a tank were positioned on a continuous weighing device and hydration was imposed by applying a water pressure of 7 kPa, corresponding to a water column of 70 cm. The water level in the column has been kept constant by adding water when necessary. Synthetic site water was introduced

Table 1 Initial conditions

Domain	"No gap" model		"Gap" model	
	Hydraulic	Mechanical	Hydraulic	Mechanical
ABCD	u_w = − 100 MPa	σ_z = 0.020 MPa, σ_r = 0.020 MPa	u_w = − 91 MPa	σ_z = 0.06 MPa, σ_r = 0 MPa
BB'C'C	–	–	u_w = − 91 MPa	σ_z = 0.06 MPa, σ_r = 0 MPa

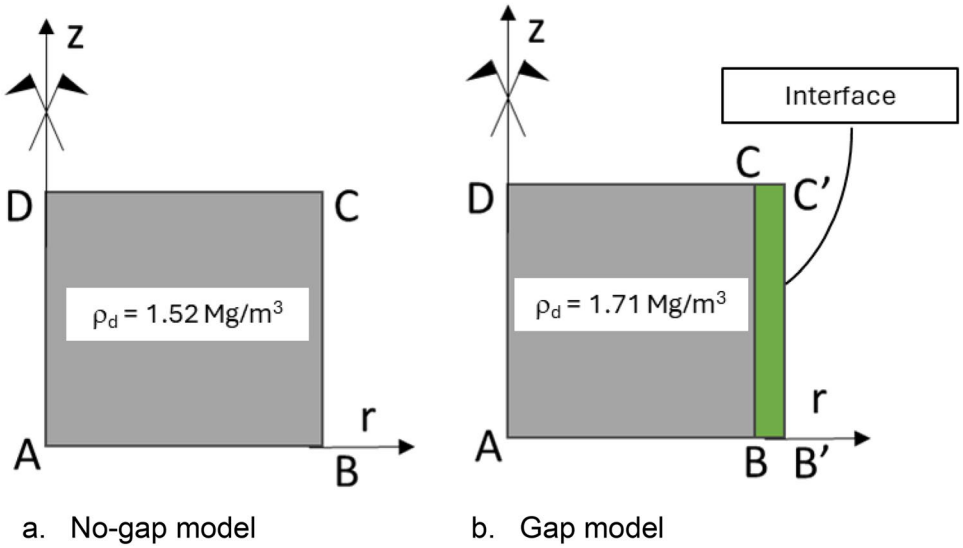

Fig. 2 Simplified schematisation of the numerical samples: (a) "no-gap" model; (b) "gap" model

in the specimen through porous plates placed at the bottom of the chamber. The synthetic water was composed of 0.281 g $NaHCO_3$, 0.426 g Na_2SO_4, 0.614 g NaCl, 0.077 g KCl, 1.082 g $CaCl \times 2H_2O$, 1.356 g $MgCl \times 6H_2O$, 0.0001 g AgCl per litre of solution. This composition resembles the Callovo–Oxfordian site porewater found at the Andra Underground Research Laboratory (Vinsot et al. 2008; Bernachy-Barbe et al. 2020).

The opposite side of the sample was maintained at laboratory conditions (controlled temperature 21 ± 1 °C.) to facilitate the evacuation of entrapped air. Further details with respect to test conditions can be found in Bernachy-Barbe et al. (2020) and Gramegna et al. (2022).

3 Numerical Model: Assumptions, Geometry, Constitutive Modelling

The numerical simulations are conducted using the finite element code LAGAMINE (Collin et al. 2002), according to the 2D axis-symmetric modelling framework introduced in Gramegna et al. (2020, 2023a), which consists in the solution of the linear momentum balance and water mass balance equations using the Barcelona Basic Model (BBM) as mechanical stress–strain relation and using a density-dependent water retention curve. The relevant equations will be recalled in Sects. 3.1, 3.2, 3.3 and 3.4. Since gas pressure is assumed to coincide with atmospheric pressure throughout the whole numerical simulation, just the equilibrium equations of the solid skeleton and the water mass balance equation are considered. The experimental test is simulated by means of two different modelling approaches:

1. "No-gap" model: in this approach, the model neglects the presence of the technological gap and just one equivalent homogeneous material is considered from the symmetry axis to the cell wall, with an initial uniform dry density of $\rho_d = 1.52 \mathrm{Mg/m^3}$, corresponding to the average dry density between the one of the bentonite block and the one of the radial gap space filled with powder. Oedometer conditions are, thus, imposed on the equivalent homogenous material disregarding the presence of the radial gap, as shown in Fig. 2a. The specimen is simulated using 25 eight-noded isoparametric elements.
2. "Gap" model: in this approach, the gap is explicitly introduced in the numerical simulation, considering the actual heterogeneity of the sample. The real initial density of the bentonite block $\rho_d = 1.75 \mathrm{Mg/m^3}$ is considered, and the presence of the radial gap filled with low-density powder is reproduced by interface elements (Fig. 2b). The sample is simulated using 800 eight-noded isoparametric elements, whilst the interface was modelled with 40 three-noded isoparametric elements.

3.1 Field Equations, Initial Conditions and Boundary Conditions

The experimental hydration test has been reproduced via the integration of two balance equations, namely the linear momentum balance and the water mass balance. The linear momentum balance equation is written as:

$$\nabla \cdot \boldsymbol{\sigma}_t + \boldsymbol{b} = 0 \tag{1}$$

where $\boldsymbol{\sigma}_t$ is the total (Cauchy) stress tensor and $\boldsymbol{b}$ is the body force vector. Water mass balance equation reads:

$$\frac{\partial}{\partial t}\left(\rho_{\mathrm{w}}\phi S_r\right)+\nabla\cdot\left(\rho_{\mathrm{w}}\boldsymbol{q_w}\right)=Q_w \tag{2}$$

where ρ_{w} is the unit weight of liquid water, ϕ is the porosity, S_r is the degree of saturation, Q_w is the external water supply, and $\boldsymbol{q_w}$ is the Darcy velocity vector, which in turn depends on the water pressure u_w gradient evolving during the hydration via:

$$\boldsymbol{q_w}=-\frac{k_{rw}\left(S_r\right)K_w}{\mu_{\mathrm{w}}}\left(\nabla u_w+\rho_{\mathrm{w}}\boldsymbol{g}\right) \tag{3}$$

being μ_{w} the water dynamic viscosity, K_w the water permeability in saturated conditions ($S_r=1$), and k_{rw} the relative permeability function. On the other hand, the air mass balance equation is not required due to the fact that the air pressure value, $\mathrm{u_a}$, is considered constant and equal to the atmospheric one during the whole development of the test.

Hydration of the samples is imposed from the bottom face (red line, Fig. 1), by assuming a linear suction decrease in 1000 s from the initial value ($s=u_a-u_w=100$ MPa for the "no gap" model and 91 MPa for the "gap" mode) to $s=-0.0068$ MPa, corresponding to a water level in the water column equal to 70 cm from the bottom of the cell. A uniform initial suction is considered for each specimen, evaluated as a function of the initial water content and the initial dry density according to the water retention model described in Sect. 3.33.3. The two models having the same initial water content $w=7.44\%$, but different initial dry densities ($\rho_{\mathrm{d}}=1.52$ Mg/m^3 for the "no-gap" model and $\rho_{\mathrm{d}}=1.75$ Mg/m^3 for the "gap" model), the initial suction is different. As for the mechanical initial conditions, in the "gap" model, a vertical stress equal to the vertical one applied in the laboratory is considered, i.e. $\sigma_z=0.06$ MPa. Due to the negligible constraint provided by the powder (as also confirmed by the experimental data shown in Figs. 3, 4, 5), the initial radial stress is set equal to zero. As for the 'no-gap' model, the rationale for the choice of the initial stress state is to have an initial mean net stress equal to the one of the "gap" model, i.e. $p=0.02$ MPa, which is the stress variable that influences the mechanical response of the BBM model. Being a null radial stress non-consistent with the modelling framework proposed in the "no-gap" approach, an isotropic initial stress is assumed, i.e. $\sigma_z=\sigma_r=0.02$ MPa. The whole set of initial and boundary conditions are summarised in Tables 1 and 2, respectively, with reference to the simplified geometrical sketch of the test shown in Fig. 2. In Table 2, w_z and w_r indicate the displacement in the vertical and radial direction, respectively.

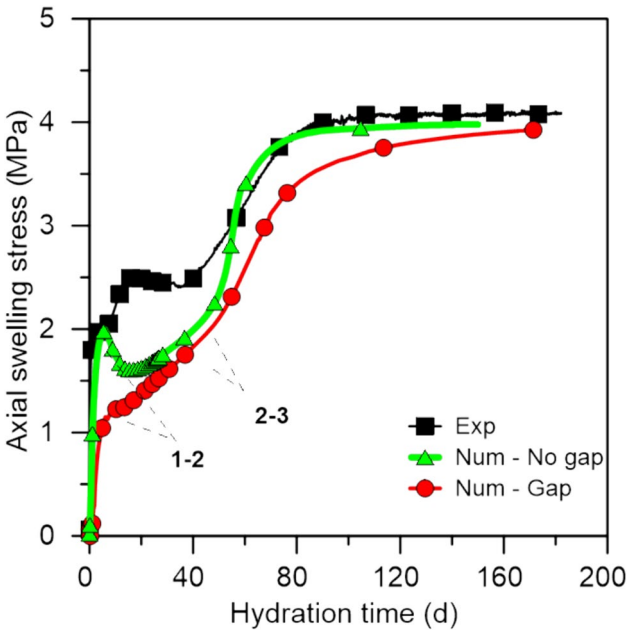

Fig. 3 Swelling stress in axial direction vs. time. Comparison between experimental data and model simulations

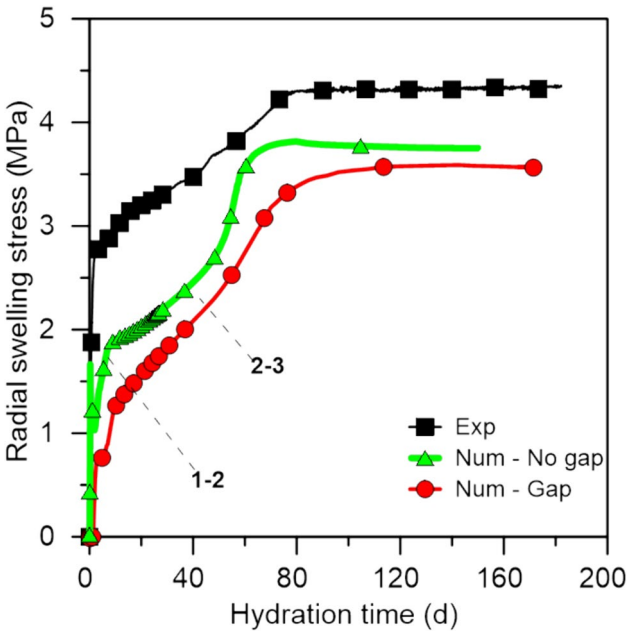

Fig. 4 Swelling stress in radial direction at $z=6.6$ mm vs. time. Comparison between experimental data and model simulations

3.2 Mechanical Constitutive Model

The stress–strain relation is here modelled via the Barcelona Basic Model (BBM) (Alonso et al. 1990), which has been already used in the literature to reproduce the mechanical response of bentonite upon hydration (see, e.g. Dieudonné et al. 2023; Toprak et al. 2017) and whose main characteristics are just briefly recalled in the following. The stress variables employed in the model are the net stress $\boldsymbol{\sigma}$ and the matric suction s, defined as the different

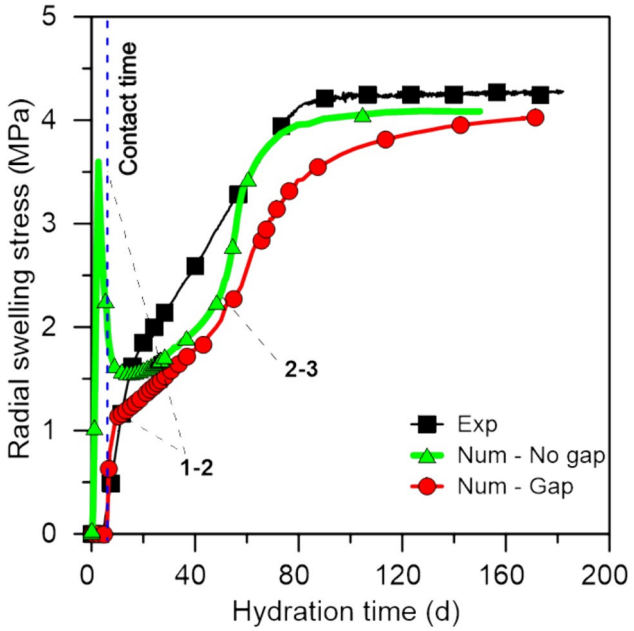

Fig. 5 Swelling stress in radial direction at $z=23.3$ mm vs. time. Comparison between experimental data and model simulations

between pore air and water pressure. The net stress is defined as

$$\boldsymbol{\sigma} = \boldsymbol{\sigma}_{\mathrm{T}} - u_a \boldsymbol{I}, \tag{4}$$

where $\boldsymbol{\sigma}_{\mathbf{T}}$ is the Cauchy total stress tensor, u_a, the air pressure, and $\boldsymbol{I}$ the identity tensor. The evolution of elastic volumetric strain is related to the mean net stress p and matric suction s changes according to (5), by means of the elastic logarithmic compressibility coefficients for changes in stress (κ) and suction (κ_s):

$$d\varepsilon_v^e = \frac{\kappa}{1+e}\frac{dp}{p} + \frac{\kappa_s}{1+e}\frac{ds}{s+u_{\mathrm{atm}}}, \tag{5}$$

where u_{atm} is the atmopheric pressure, equal to 0.1 MPa. To reproduce the hydromechanical response of expansive clays, the original model can also be modified to incorporate the stress dependency of wetting-induced swelling strain (Dueck and Nilsson 2010), as shown in (6), where the dependence of κ_s on the mean net stress is introduced:

$$\kappa_s(p) = \kappa_{s0} * \exp\left(-\alpha_p * p\right), \tag{6}$$

where κ_{s0} is the elastic logarithmic compressibility coefficients for changes in suction at null mean stress and α_p is a parameter that rules the dependence of κ_s on the applied stress. The increase of preconsolidation pressure (p_0) with respect to suction (s) is introduced to model the expansion of the elastic domain with suction (7), together with the change of the elasto-plastic compressibility coefficient ($\lambda(s)$) with suction (8):

$$p_0(s) = p_c\left(\frac{p_0^*}{p_c}\right)^{\frac{\lambda(0)-\kappa}{\lambda(s)-\kappa}} \tag{7}$$

$$\lambda(s) = \lambda(0)\left[(1-r)\exp(-\omega s) + r\right] \tag{8}$$

3.3 Water Retention Model

The water retention model presented in Dieudonné et al. (2013, 2017) is used in this study. Accordingly, the water ratio (e_w), which is defined as the product of the void ratio (e) and the degree of saturation (S_r), is split into two additive components: the water ratio adsorbed in the micropores (e_{wm}) and the water ratio stored in macropores (e_{wM}), which in turn depend on suction:

$$\begin{aligned} e_{\mathrm{wm}} &= e_m \exp\left(-\left(C_{\mathrm{ads}} s\right)^{n_{\mathrm{ads}}}\right) \\ e_{\mathrm{wM}} &= \left(e - e_m\right)\left[1 + \left(\frac{s}{A}\left(e - e_m\right)\right)^n\right]^{-m} \end{aligned} \tag{9}$$

C_{ads} and n_{ads} are two material parameters related to retention properties of the micropores. The parameter n_{ads} controls the curvature of the water retention curve in the high suction range, whilst C_{ads} is associated with the air-entry (or air-occlusion) suction of the intra-aggregate voids. A, m, n are the material parameters related to the retention properties of the macropores, according to the classical van Genuchten formulation. In particular, A controls the dependence of the air-entry pressure on the macrostructural void ratio.

Table 2 Boundary conditions

	L [mm]	"No gap" model		"Gap" model	
		Hydraulic	Mechanical	Hydraulic	Mechanical
AB/AB'	28.5	$u_w = 6.86$ kPa	$w_z = 0$	$u_w = 6.86$ kPa	$w_z = 0$
BC	45	$q_{wx} = 0$	$w_r = 0$	$q_{wx} = 0$	
B'C'	45			$q_{wx} = 0$	$w_r = 0$
CD/C'D	28.5	$u_w = 0$ kPa	$w_z = 0$	$u_w = 0$ kPa	$w_z = 0$
DA	28.5	$q_{wx} = 0$	$w_r = 0$	$q_{wx} = 0$	$w_r = 0$

Table 3 Parameters and initial values of the internal variable for the BBM model

Symbol	Unit	Meaning	Value	
κ	[−]	Elastic compressibility coefficient for changes in mean net stress	0.03	
κ_{s0}	[−]	Elastic compressibility coefficient for changes in suction	No-gap 0.220	Gap 0.250
α_p	[MPa^{-1}]	Parameter controlling the stress dependency of the swelling strain for change in suction	3.5×10^{-1}	
p_0*	[MPa]	Pre-consolidation pressure for saturated state	0.3	
p_c	[MPa]	Reference pressure controlling the shape of the LC curve	0.086	
$\lambda(0)$	[–]	Slope of the saturated virgin compression line	0.25	
r	[–]	Parameter defining the minimum soil compressibility	0.32	
ω	[MPa^{-1}]	Parameter controlling the soil stiffness	0.51×10^{-1}	
M	[–]	Critical state obliquity	20	
ν	[–]	Poisson ratio	0.17	
$c(0)$	[MPa]	Cohesion in saturated conditions	0.10	
k	[–]	Parameter controlling the increase of cohesion due to suction	0.0046	

The model also accounts for the evolution of aggregate size with changes in water content, according to:

$$e_m = e_{m0} + \beta_0 e_w + \beta_1 e_w^2, \tag{10}$$

where e_{m0}, β_0 and β_1 are model parameters. In particular, e_{m0} is the microstructural void ratio for the dry material ($e_w = 0$), and β_0 and β_1 are parameters that quantify the swelling potential of the aggregates. The differentiation between micropores and macropores was based on experimental observations and theoretical interpretations presented in the works of Romero et al. (2011) and Della Vecchia et al. (2015).

3.4 Permeability Model

The saturated water permeability evolution was determined by employing an extended Kozeny–Carman model, which considers the presence of both micropores and macropores in compacted bentonite-based materials. As suggested by Romero (2013) and Gramegna et al (2023b), the macro-void ratio e_M (expressed as $e_M = e - e_m$) was used to replace the total porosity in the original model:

$$K_w = C_k \frac{e_M^N}{\left(1 - e_M\right)^N} \tag{11}$$

where C_k is a reference permeability and N is a parameter that controls the dependence on the macro-void ratio. This model allows predicting the reduction in permeability upon isochoric conditions, characterised by a constant value of e and an increase of e_m according to (10). The dependence of the relative permeability and S_r is expressed by a power law, where the exponent γ is a model parameter:

$$k_{rw} = S_r^\gamma \tag{12}$$

3.5 Material Parameters

The mechanical parameters of BBM (see Table 3) have been calibrated on both swelling and consolidation tests in isotropic conditions performed by Tang et al. (2008) on MX80 bentonite, compacted at $\rho_d = 1.78$ Mg/m^3 and $w = 10\%$. The detailed calibration procedure is reported in Gramegna (2021). All the parameters presented in Gramegna et al. (2020) are kept also for the simulation reported in the present paper, except κ and κ_{s0}. In particular, κ has been recalibrated to obtain better predictions in the relevant dry density range, whilst κ_{s0} has been adjusted to account for the dry density dependence of the swelling strain, which is not covered by Eq. 6. In this way, it is possible to focus the attention on comparing the development of swelling strain upon hydration in the intermediate hydration stage, once the final swelling strain is well caught. It is worth noting that κ_{s0} is the only parameter that is different for the "gap" and the "no gap" model. The parameters for Eq. 10 have been taken from Dieudonnè et al. (2017), who exploited experimental data presented in Delage et al. (2006), Wang (2012) and Seiphoori et al. (2014).

The same set of water retention curve parameters are used for both the "gap" and the "no-gap" models, due to the built-in capability of the Dieudonné et al. (2017) model to account for different dry densities, as shown in Table 4. The parameters governing the water permeability evolution (Table 5) has been calibrated by best fitting the evolution of water content during the first inflow stage.

Table 4 Parameters of water retention model

Symbol	Unit	Meaning	Value
e_{m0}	[–]	Microstructural void ratio for the dry material	0.31
β_0	[–]	Parameters quantifying the swelling potential of the aggregates	0.1
β_1	[–]		0.48
C_{ads}	[MPa^{-1}]	Parameter associated to the air-entry pressure of micro-voids	0.0075
n_{ads}	[–]	Parameter controlling the WRC curvature in the high suction range	0.2
n	[–]	Material parameters	3
m	[–]		0.45
A	[MPa]	Parameter controlling the dependence of the air-entry pressure on the macrostructural void ratio	0.2

Table 5 Parameters of the permeability model

Symbol	Unit	Meaning	Value
C_k	[m^2]	Reference permeability	1.8×10^{-20}
N	[–]	Model parameters	0.4
γ	[–]	Parameter controlling the evolution of relative permeability	2

Table 6 Interface mechanical properties

Symbol	Unit	Meaning	Value
K_N	[N/m^3]	Penalty coefficient in the normal direction	3×10^9
K_T	[N/m^3]	Penalty coefficient in the longitudinal direction	3×10^9
φ_i	[°]	Interface friction angle	0
c'_i	[MPa]	Interface cohesion	0

3.6 Interface Model

The initial radial gap is simulated in the "gap" model via the hydromechanical zero-thickness element implemented in LAGAMINE (see Cerfontaine et al. 2015), by employing 40 3-noded isoparametric elements (green line Fig. 2). Being the cell wall very rigid, it acts a normal constraint for the swelling bentonite block, whilst, in the tangential direction, the material is vice versa considered free to slide, and thus interface friction and cohesion are neglected. As for the hydraulic behaviour of the interface, the experimental evidence excludes the presence of concentrated water flow along the interface, probably due to the swelling of the bentonite block upon wetting and the presence of the powder. As a consequence, the interface model is set to prevent water flow in the gap, along both the normal and the tangential directions. The block–wall interaction is reduced to a merely mechanical interaction. The formulation of the interface element is summarised in Appendix A. The interface mechanical parameters used in the simulation are given in Table 6 (please refer to Appendix A for the description of the parameters). The initial gap thickness g_N ($t=0$) has been set equal to 2.1 mm (see also Fig. 1). In particular, the choice of the appropriate penalty coefficients K_N and K_T is crucial: in fact, if the penalty coefficients are too small, the constraints may not be adequately enforced, leading to inaccurate results. Conversely, if the penalty coefficients are too large, they can lead to ill-conditioning of the system equations and numerical instability (Li and Zhang (2015)). Following the approach proposed by Cerfontaine (2014), the penalty coefficients were selected as 3×10^9 N/m^3.

4 Numerical Results and Comparison with Experimental Data

4.1 Stress Evolution During Hydration Process

Figure 3 shows a comparison between the experimental data and the numerical predictions of the evolution of the axial stress over time throughout the whole experimental test. According to the experimental data, the two numerical simulations evidence three stages, which can be linked to the elasto-plastic mechanical behaviour of the swelling soils:

1. Initial rapid increase of swelling pressure related to the elastic response of the material;
2. Slower increase, or even a decrease, of the swelling pressure, once the yield locus is reached;
3. A final swelling pressure increase, up to a final stationary value.

The initial swelling axial stress development occurs with a higher rate in the "no-gap" model compared to the "gap" approach. This discrepancy primarily stems from the different radial constraints applied in the two models, which influence the effective stress path and thus the intersection with the yield surface. The second stage occurs once the yield locus is attained: the different material stiffness results in a significant change in the swelling pressure evolution. Remarkably, both the models are able to reproduce the gradual decrease of the rate of swelling pressure development.

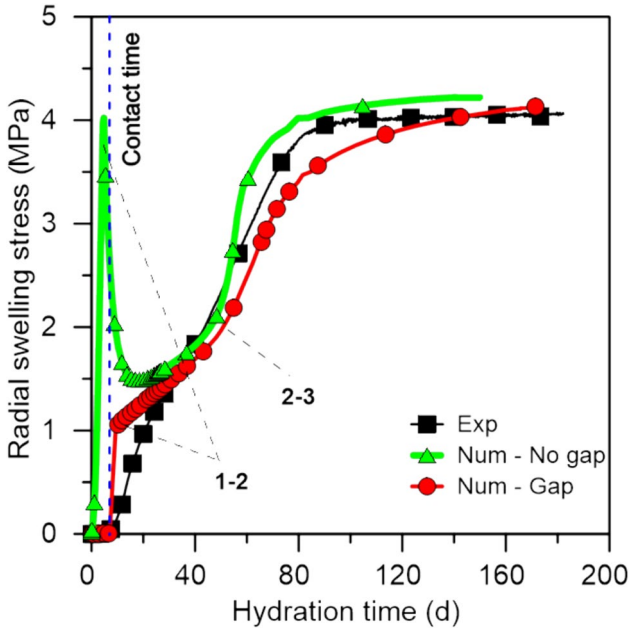

Fig. 6 Swelling stress in radial direction at $z=40$ mm vs. time. Comparison between experimental data and model simulations

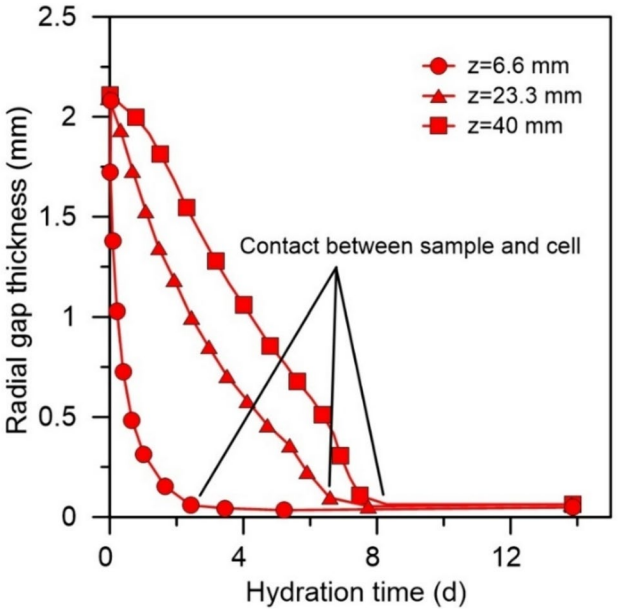

Fig. 7 Radial gap thickness at several heights z as function of time ("gap" model)

The third stage is characterised by low suction, high degree of saturation and a final swelling pressure increase: again, both the models are able to reproduce the experimental data satisfactorily. The boundaries of the stages are indicated in Figs. 3, 4, 5 and 6 with the symbols:

- "1–2", corresponding to the end of stage 1 and the beginning of stage 2;
- "2–3" corresponding to the end of stage 2 and the beginning of stage 3.

Differences between the numerical results of the "gap" model and the experimental data are evident especially during stage 1, where the rate of axial strain increase predicted by the model is lower than the experimental one. Due to the calibration procedure, the final swelling axial stress is very similar to the experimental one, corresponding approximately to 4.1 MPa. The time evolution of the radial stress shows similar characteristics to the evolution of the axial stress, as shown in Figs. 4, 5 and 6, where the radial stress is measured at three different heights z from the bottom end of the sample, namely 6.6 mm, 23.3 mm and 40 mm. In terms of radial swelling stress evolution upon hydration, the predictions of the "no-gap" model for the points located at a larger distance from the hydration face ($z=23.3$ mm and 40 mm, Figs. 5 and 6) are characterised by a marked peak, followed by an abrupt stress decrease. The peak is absent in the simulations performed with the "gap" model. After 20 days, the predicted values by both the models match the experimental data in a satisfactory way, both from the qualitative and the quantitative point of view, and the final swelling stress is well reproduced.

To have an insight on the numerical predictions of the "gap" model, the time evolution of the radial gap thickness at various locations is shown in Fig. 7. From the experimental point of view, the gap is defined as the normal distance between the cell wall and the sample. The initial gap thickness is related to the initial geometrical configuration, as the difference between the cell radius (28.5 mm) and the sample radius (26.4 mm), i.e. 2.1 mm (see Figs. 1 and 2b). This value is necessary to initialise the gap function g_N ($t=0$). As long as the simulation proceeds, the current value of the radial gap thickness coincides with the current value of g_N, updated according to Eq. 13. The radial gap thickness evolution, i.e. the distance between the bentonite sample side and the cell wall, enables evaluating the 'time of contact', namely the time corresponding to the closure of the gap, as well as the deformation kinetics. At $z=6.6$ mm, closure of the gap occurs after 3 days since the beginning of the hydration process, whilst it occurs at day 7 and day 8 at $z=23.3$ mm and $z=40$ mm, respectively. Before the time of contact, the void ratio evolution in time for the "gap" model exhibits an initial increase, corresponding to swelling in the radial direction (not reported here for the sake of brevity). It is worth noting that the predictions of the "gap" and the "no-gap" models shown in Figs. 5 and 6 differ significantly for time lower than the time of contact (indicated with a blue vertical dashed line), i.e. when the deformation responses of the specimens are different according to the different

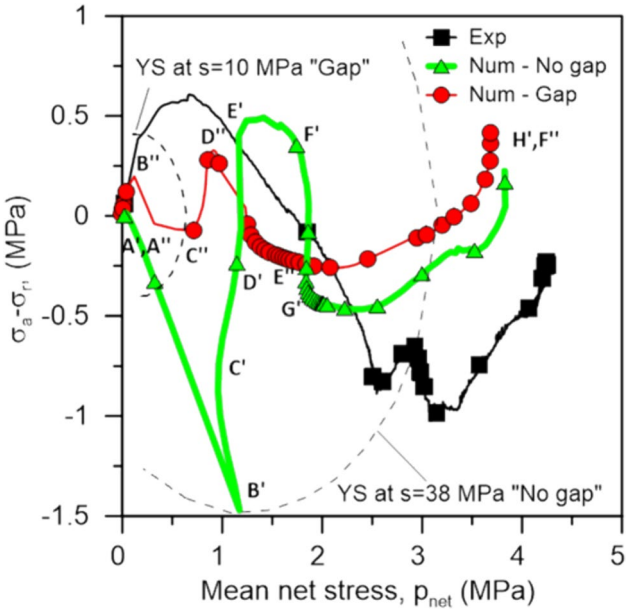

Fig. 8 Stress path in the $(\sigma_a - \sigma_r)-q$ plane for the point located at $z=6.6$ mm from the hydration face. Comparison between experimental data and model simulations

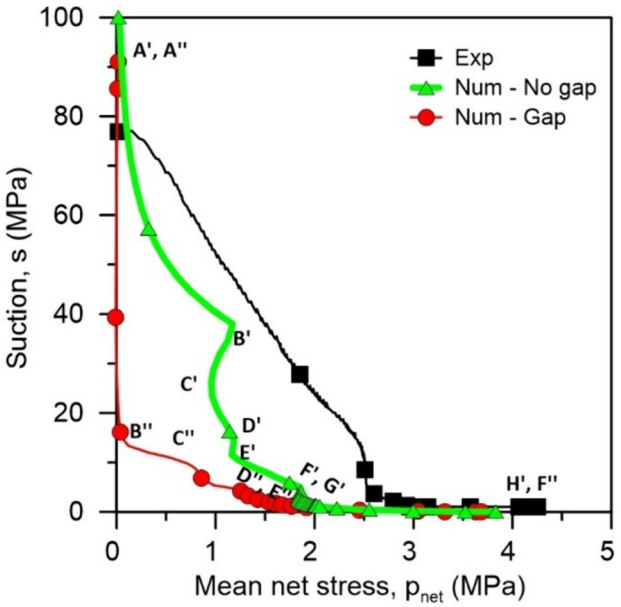

Fig. 9 Stress paths in the $p_{net}-s$ plane for point located at $z=6.6$ mm from the hydration face. Comparisons between experimental data and model simulations

kinematic constraints. Subsequently, when contact between the cell wall and the specimen side is completely developed, the model predictions of the "no-gap" and the "gap" models tend to converge.

4.2 Stress Paths

To gain a deeper understanding and to clarify the different predictions of the two numerical models, the stress paths corresponding to a point located at z = 6.6 mm on the symmetry axis of the specimen are shown in Fig. 8, in the plane $(\sigma_a–\sigma_r)$ vs. net mean stress p_{net} (being σ_a and σ_r the axial and radial stress, respectively), Fig. 9 (suction s vs. mean net stress p_{net}), Fig. 10 (void ratio e vs. suction s) and Fig. 11 (axial stress vs. radial stress), following the approach presented in Dieudonné et al. (2023).

4.2.1 "No-gap" Model

– From A' to B': the suction decrease imposed at the bottom face causes a local volume increase, whilst the whole sample is characterised by global isochoric conditions. As long as hydration takes place from the bottom, suction decreases, the degree of saturation increases and both the axial and the radial swelling stress develop. The radial stress evolution rate is larger than the axial one, due to the one-dimensional hydration conditions from the bottom end: despite isochoric conditions hold globally, local swelling is allowed in the axial direction, but not in the radial one. This causes an almost linear stress path in the $(\sigma_a–\sigma_r)-p_{net}$ plane, with an inclination −1.31, which is slightly smaller than − 1.5 (i.e. the inclination of the stress path in oedometer conditions at constant axial stress). The material behaviour up to point B' is elastic.

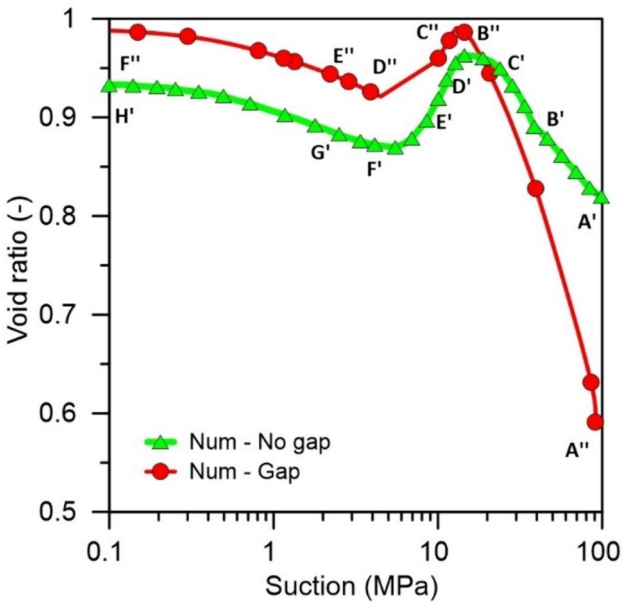

Fig. 10 Stress paths in the $e-s$ plane for point located at $z=6.6$ mm from the hydration face. Comparisons between model simulations

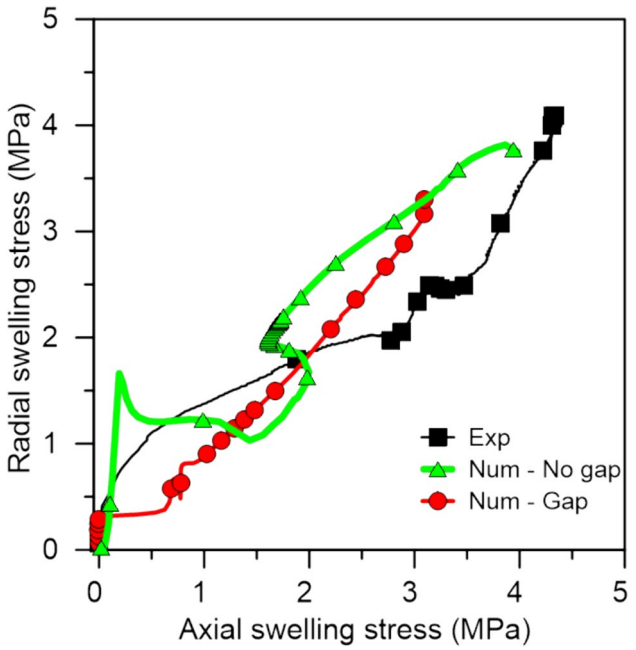

Fig. 11 Stress paths in the $\sigma_a - \sigma_r$ plane for point located at $z = 6.6$ mm from the hydration face. Comparisons between experimental data and model simulations

- From B' to C': in B', the stress path reaches the yield surface. The elastic swelling upon hydration is still present, together with a dilatant plastic strain increment related to the current stress obliquity, which is associated with material softening. Despite locally the material swells as a whole (local void ratio increase), the effect of the development of deviatoric plastic strain is a reduction of p_{net} and an increase in $(\sigma_a - \sigma_r)$. Along the whole B'C' path, the stress state remains on the yield surface, which is in turn reducing in size. In point C', the net mean stress reaches a local minimum.
- From C' to D': again, the hydration mechanism continues to induce elastic volumetric expansion, but the stress obliquity is such that compressive volumetric plastic strain also develops. This induces a slight expansion of the yield surface, together with an increase in net pressure and again a local void ratio increase. In point D', the difference between the axial and the radial stress is almost equal to zero and the stress state almost lies on the Loading Collapse curve.
- From D' to E': compressive volumetric strain upon hydration (also known as wetting-induced collapse) develops. This contribution starts to be more relevant than the elastic swelling due to suction reduction. The global effect is a local void ratio reduction, associated with a further increase in $(\sigma_a - \sigma_r)$ and a negligible change in p_{net}, indicating a higher axial swelling stress than the radial one. In point E', the size of the yield surface is minimum and the material is still unsaturated ($s = 10$ MPa, Sr = 68%).
- From E' to F': the material point is still subjected to wetting, but the advancement of the hydration front is such that the points placed above $z = 6.6$ mm starts in turn to swell. Due to the global isochoric conditions, the effect of the swelling of the upper layers is a mean stress increase, associated to a local void ratio reduction (compaction) in $z = 6.6$ mm, at almost constant $(\sigma_a - \sigma_r)$. In point F', the maximum reduction in void ratio is achieved.
- From F' to G': the further reduction in suction implies a slight increase in void ratio, due to the lower tendency of the upper layers to swell. As a consequence, $(\sigma_a - \sigma_r)$ starts to decrease again, upon point G'.
- From G' to H': material hydration continues with relevant development of axial swelling stress, until the sample reaches full saturation.

4.2.2 "Gap" Model

- From A'' to B'': the reduction in suction applied at the bottom face induces elastic volumetric expansion. Unlike the "no-gap" case, the material can swell locally in both the axial and radial directions. As a whole, the bentonite block is subjected to a constrain in the development of a global axial strain, whilst the global radial strain is prevented just when the contact between the block side and the cell wall is completely developed. As a consequence, the hydration induces an increase in the axial swelling stress, whilst the radial net stress remains null until the block is not in contact with the cell wall. The stress path in the $(\sigma_a - \sigma_r) - p_{net}$ plane exhibits a slope almost equal to 3, corresponding to a purely axial compression path. At this stage, the increase in axial stress is lower than 0.25 MPa (see Fig. 3). At B'', the block comes in contact with the cell wall in the radial direction and the free radial swelling condition switches to a local oedometer condition. The stress point in B'' is still inside the yield surface.
- From B'' to C'': during this stage, radial strain in $z = 6.6$ m is prevented. As a consequence, radial swelling stress starts to develop and $(\sigma_a - \sigma_r)$ starts to decrease. The inclination of the stress path is − 1.34 in the $(\sigma_a - \sigma_r) - p_{net}$ plane, which is close to what expected for swelling in oedometer conditions. Despite the reduction in suction and the purely elastic response (which would induce material swelling), the local void ratio decreases, due to the effect of the hydration and swelling of the upper layers which causes local compression at the considered depth, as testified by the increase in p_{net}. During this stage, material behaviour is still elastic. In point C'', the stress path reaches the yield surface.

- From C'' to D'': suction decrease promotes elastic swelling volumetric strains (via Eq. 5), whilst the current stress state obliquity together with the increase of p_{net} induces compressive volumetric plastic strains, according to the flow rule. The plastic volumetric compression induces a lower increase of radial stress, and thus to an increase of (σ_a–σ_r). During this stage, the size of the yield surface is increasing. For the sample as a whole, see Fig. 3, the local void ratio reduction is, however, hindered by the swelling of the upper layers, which induces a continuous increase of the axial swelling stress. In point D'', the local void ratio reaches a minimum.
- From D''E'': the hydration continues and the deformation mechanism comes to be again just elastic, with an increase in radial stress and a decrease in (σ_a -σ_r).
- From E'' to F'': as the material is hydrated, significant volume changes occur locally at various heights of the sample. The mean net pressure keeps raising until the sample reaches full saturation. Throughout this stage, (σ_a–σ_r) experiences first a decrease, followed by an increase similar to the one of the "no-gap" model.

5 Discussion

In Sect. 4, the numerical results of two distinct modelling strategies, namely the "no gap" and "gap" models, have been employed to get an insight into the hydromechanical behaviour of compacted bentonite, with a particular focus on the role of the presence of technological gaps during intermediate saturation stages. The two models are calibrated to correctly reproduce the final axial swelling stress. The "no-gap" model is not able to reproduce the whole experimental evidence: despite satisfactory predictions are obtained in terms of axial stress and in terms of radial stress evolution near the hydration boundary, the radial stress time evolution at higher locations—differently from the experimental data—is characterised by a sudden increase, followed by a decrease and a final increase up to stabilisation. Since the numerical approach of the "no gap" model considers isochoric conditions since the beginning of the simulation (i.e. the radial gap between the block and the cell wall is disregarded), it fails to capture all the aspects related to the initial possibility of the specimen to develop radial strains, largely overestimating the rate of radial stress increase in some locations. The very high initial radial pressure peak predicted by the "no gap" model can be, thus, related to the different stress path followed, which in turn impacts on the subsequent plastic response. As for the "gap" model, both axial and radial swelling stress evolve with time in a non-linear monotonic way upon hydration. Despite the prediction near the hydration boundary in terms of radial stress is comparable, if not slightly worse, to the "no gap" model, radial swelling stress predictions do not show any peak during the early hydration stage (e.g. day ~ 4, see Figs. 5 and 6). Moreover, at day 4, radial swelling stress is still zero at $z = 23$ mm and $z = 40$ mm, because the contact between the bentonite block and the cell wall has not been established yet. Also in the following stages, the "gap" model reproduces well the experimental results, both in terms of final swelling stress magnitude and kinetics. This aspect is particularly relevant, because the information about stress development in engineered barriers during the whole hydration process is a fundamental input for good design practises of in situ facilities. Stress development is in fact related not only to the creation of good sealing and to fracture closure, but also to the possibility of further damaging of the host-rock's EDZ or of the containing concrete liners, and thus to the creation of preferential pathways for radionuclides.

The comparison between the stress paths in the $p_{net}-s$ plane at $z = 6.6$ mm (Figs. 8 and 9) is also insightful. The experimental results appear consistent with a constant volume hydration, probably due to an already developed contact between the cell wall and the bentonite block related to the specimen preparation procedure (i.e. implying that the contact with the cell wall and the block has already taken place, possibly due to the accumulation of bentonite powder at the bottom of the gap). Consistently, the "no-gap" model seems to better reproduce the experimental results. Conversely, for $z = 40$ mm (Figs. 12 and 13), the experimental stress path appears consistent with the presence of the gap, mostly similar to one of the swelling at constant stress, as correctly reproduced by just the "gap" model, whilst the "no gap" one seems neither to get, from a qualitative point of view, the physical process.

As a further comparison between the modelling approaches, Fig. 14 shows the spatial evolution of radial stress for the same hydration time, compared with the experimental data. The evolution with sample height observed in the experimental results during the early stages of hydration ($t < 7$ days) is well reproduced by "gap" model. According to Fig. 14, at day 4.7, since the beginning of the test, a radial stress of 2.7 MPa was measured at $z = 6.6$ mm, whilst the sensor placed at $z = 40$ mm did not measure any change. Though both "gap" and "no-gap" model underestimate the experimental radial swelling stress value at $z = 6.6$ mm, the "gap" model is capable of predicting the negligible radial swelling stress for at $z > 23$ mm, which is largely overestimated by the "no gap" model. At day 7, despite the "no-gap" model has already passed the predicted peak in radial stress (see Figs. 4, 5, 6) and it is on the descending branch for every height, it still overestimates the experimental radial swelling stress. Again, the prediction of the "gap" model is better from the qualitative point of view. As the hydration time progresses, the radial stress distributions of the two models tend to coincide (see day 105 in Fig. 14), as long as

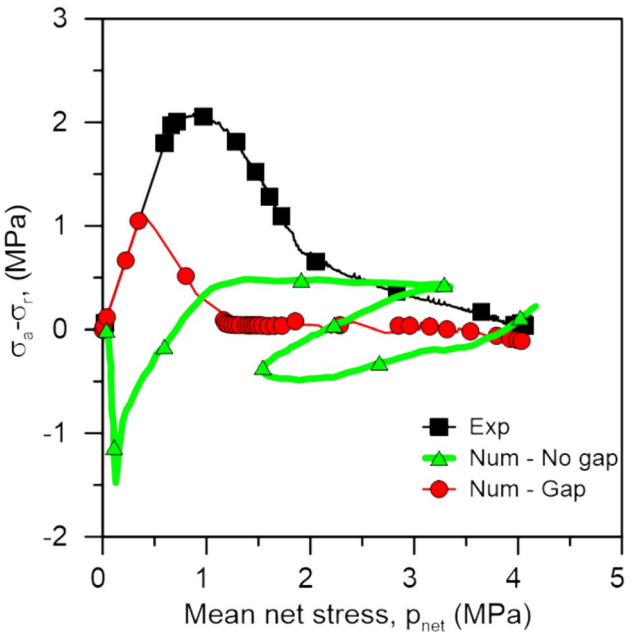

Fig. 12 Stress path in the $(\sigma_a - \sigma_r) - p_{net}$ plane for point located at $z = 40$ mm from the hydration face. Comparison between experimental data and model simulations

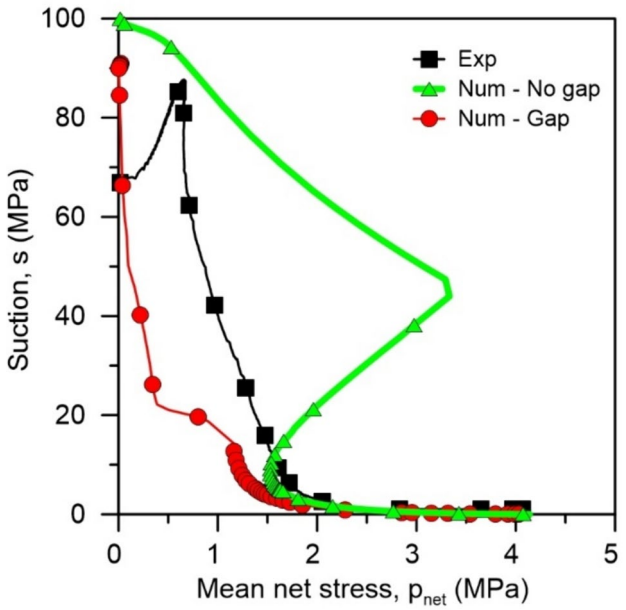

Fig. 13 Stress paths in the p_{net}–s plane for point located at $z = 40$ mm from the hydration face. Comparisons between experimental data and model simulations

the radial stress develops in both models with the advancement of the hydration.

6 Conclusion

This work focuses on the investigation of the role of technological gaps upon bentonite hydration, which holds utmost significance in the realm of successful engineered barrier design and performance assessment for nuclear waste disposal. The presence of these gaps can indeed exert substantial influence on the hydromechanical behaviour of bentonite-based materials, not only in terms of preferential pathways for the migration of water, gas and radionuclides, but also in terms of stress development upon hydration. In this study, an experimental test consisting in the hydration of a compacted bentonite sample in oedometer condition is reproduced by two different numerical modelling strategies, named "no-gap" and "gap" models. The test is characterised by the presence of a technological gap between the compacted sample and the cell wall and by the application of a constraint in terms of vertical displacements. The "no-gap" model is essentially a simplified representation of an equivalent uniform medium (where the localised gap is not modelled, but an average density is considered) subjected to isochoric hydration conditions: the absence of an explicit model for the gap implies a full contact between the compacted bentonite and the cell wall since the beginning of the hydration. The "gap" model vice versa explicitly considers the presence of the gap and the real geometry of the bentonite block, reproducing the interface with ad-hoc finite elements.

The outcomes of the two proposed modelling strategies were thoroughly examined and compared with experimental data not only in terms of time evolution of swelling pressure—as in most of the technical papers on the subject—but also in terms of mean net stress vs. suction, void ratio vs. suction, and remarkably in terms of stress paths at different heights. All that information provides an enhanced understanding on the phenomena taking place during bentonite isochoric hydration with both "no-gap" and "gap" models. In particular, this work highlights the relevance of the complex effects of the radial gap on the mechanical response upon hydration, especially with respect to the initial and intermediate hydration phases. The analyses performed highlight the fact that the existence of a localised void space influences the development of swelling stress at the beginning of the hydration stage, with relevant effects on the stress path direction and consequently the intersection with the yield surface. The "gap" numerical model provides remarkable good predictions of the experimental results during the whole test development. On the other hand, the disregard of the existing gap ("no gap" model) leads to strong overestimation of the radial swelling stresses in some locations during the early hydration phase, which makes their use less reliable for nuclear waste disposal facilities, especially at the beginning of the repository's life. In fact, when the nuclear waste is at

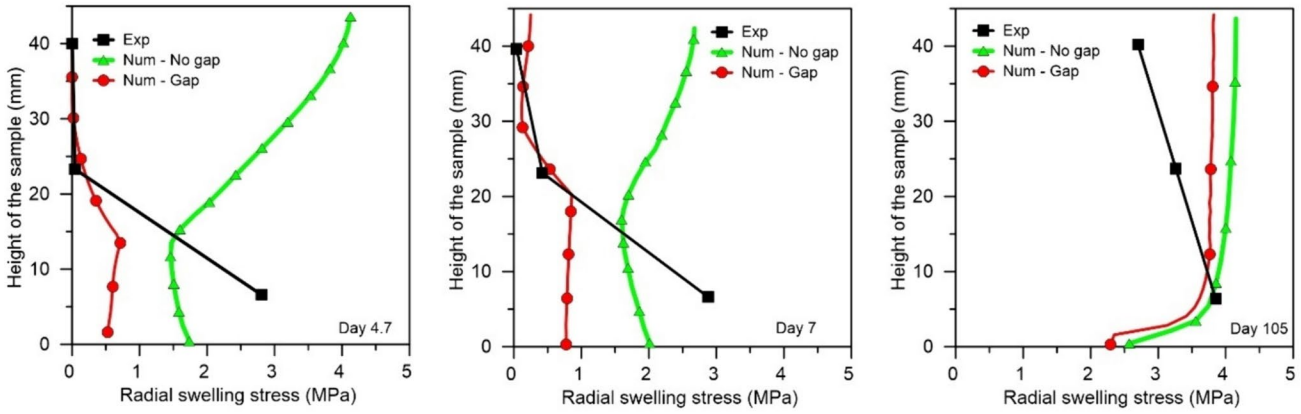

Fig. 14 Radial swelling pressure profiles at several times (from left to right days: 4.7, 7 and 105): comparison between experimental data and model simulations

the maximum of its radioactivity, the bentonite structure is expected to effectively seal and close the fractures within the excavation damaged zone, which may serve as preferential pathways for radionuclides, ensuring at the same time that its swelling stress does not overcome the natural stress levels of the geological formation. Thus, swelling stress-reliable prediction during every phase of disposals use, which spans for tens of centuries, is of paramount importance for its short-term and long-term stability assessment.

A conscious employment of numerical models for bentonite materials in underground facilities is also fundamental for the design of the layouts of blocks: it has been in fact proved that, if the full contact is established since the very beginning of the hydration to limit preferential pathways for radionuclides migration, large stress peaks may be achieved, potentially exceeding the natural stress level of the geological formation, causing extreme damage. On the other hand, configurations in which technological gaps exist at the beginning of the nuclear waste emplacement may be dangerous with respect to the risk of radioactive substances leakage, but inducing lower stress values and reducing the risk related to the interaction with the geological host rocks and gallery liners.

Appendix A

Interface Element

See (Eqs. 13–19) here.

The hydromechanical zero-thickness element implemented in LAGAMINE (Cerfontaine et al. 2015) is here briefly described with regard to its application in this study. The element classification is limited to two-dimensional analysis under isothermal conditions, as well as, in its mechanical characteristics. Two deformable porous bodies denoted $\mathcal{B}_1$ and $\mathcal{B}_2$, in their current configuration at time t, are considered in the description of a general mechanical problem. Between $\mathcal{B}_1$ and $\mathcal{B}_2$, a gap function can be defined, denoted g_N:

$$g_N = \left(\boldsymbol{x}^2 - \boldsymbol{x}^1\right) \cdot \boldsymbol{e}_1, \tag{13}$$

where $\boldsymbol{x}^1$ represents the projection of the point $\boldsymbol{x}^2$ belonging to the boundary of $\mathcal{B}_2$ on the closest point on the boundary of $\mathcal{B}_1$. $\boldsymbol{e}_1$ is a unit normal vector at point x^1. If there is no contact, g_N is positive; for g_N equal to zero, the contact is termed ideal (i.e. contact without interpenetration of the solid bodies); for negative g_N, an interpenetration distance can be defined. Interpenetration is necessary to produce contact pressure when the penalty method is used. Contact between two solids induces non-zero stress vectors $\boldsymbol{\sigma}_c$ along their common boundary. The vector $\boldsymbol{\sigma}_c$ is described in the corresponding local system of coordinates at each contacting point such that:

$$\boldsymbol{\sigma}_c = -p_N \boldsymbol{e}_1 + \tau \boldsymbol{e}_2 = \begin{bmatrix} -p_N & \tau \end{bmatrix}^T, \tag{14}$$

where p_N is the normal pressure and τ is the shear stress in the plane of the interface and $\boldsymbol{e}_2$ is the unit tangential vector at point x^1. According to the penalty method, in case of contact, the relation between the pressure and the gap function reads:

$$\dot{p}_N = -K_N \dot{g}_N, \tag{15}$$

where the minus sign ensures a positive increment of contact pressure when interpenetration occurs, i.e. $g_N < 0$ and $\dot{g}_N < 0$. If the penalty method is employed, interpenetration is necessary to generate contact pressure and the gap function becomes negative. When the solids are in contact, the ideal tangential behaviour of the interface distinguishes between

the stick and slip states. In the stick state, two points in contact are not allowed to move in the tangential direction, so that the increment in the tangential relative displacement is null, i.e. $\dot{g}_T = 0$, and they keep stuck together. On the other hand, in the slip state, a relative tangential displacement g_T exists between both sides of the interface. From a computational point of view, once a plasticity criterion $f_c(\sigma_c)$ is defined (identifying a threshold of admissible shear stress):

$$\dot{g}_T^{sl} \geq 0 \quad f_c(\sigma_c) \leq 0 \quad \dot{g}_T^{sl} f_c(\sigma_c) = 0, \tag{16}$$

where $\dot{g}_T^{sl}$ is the variation of the non-recoverable displacement in the tangential direction, which is related to the variation of tangential displacement by:

$$\dot{g}_T = \text{sign}(\dot{\tau}) \dot{g}_T^{sl}, \tag{17}$$

with $\text{sign}(\dot{\tau})$ the sign function of $\dot{\tau}$. In this work, the Coulomb frictional criterion is adopted as plasticity criterion:

$$f_c(\boldsymbol{\sigma}_c) = |\tau| - c'i - p_N \tan \varphi_i, \tag{18}$$

where $|\tau|$ is the norm of the shear stress τ, and c'_i and φ_i are the interface cohesion and friction angle, respectively. Furthermore, perfect plasticity is considered at the interface: once that the Coulomb criterion is reached, relative displacement of the interfaces continues without any further increase of the shear stress, unless the normal stress is increased. The penalty method allows also relative elastic displacement for the stick state. Shear stress and tangential variation of displacement are linked linearly by the penalty coefficient K_T :

$$\dot{\tau} = K_T \dot{g}_T. \tag{19}$$

Acknowledgements The authors would like to express their sincere gratitude to the Beacon project (Grant Agreement ID 745942) for its funding.

Funding This article is funded by Horizon 2020, 745942.

Data Availability Data will be made available on request.

Declarations

Conflict of interest The authors have no relevant financial or non-financial interests to disclose.

References

Alonso EE, Gens A, Josa A (1990) A constitutive model for partially saturated soils. Géotechnique 40(3):405–430

Alonso EE, Hoffmann C, Romero E (2010) Pellet mixtures in isolation barriers. J Rock Mech Geotech Eng 2(1):12–31

Alonso EE, Vaunat J, Gens A (1999) Modelling the mechanical behaviour of expansive clays. Engineering geology 54(1-2):173–183

Baryla P, Bernachy-Barbe F, Bosch JA, Campos G, Carbonell B, Daniels KA. Wieczorek K (2019) Bentonite mechanical evolution–experimental work for the support of model development and validation. Technical report, Beacon

Bernachy-Barbe F (2021) Homogenization of bentonite upon saturation: density and pressure fields. Appl Clay Sci 209:106122

Bernachy-Barbe F, Conil N, Guillot W, Talandier J (2020) Observed heterogeneities after hydration of MX-80 bentonite under pellet/powder form. Appl Clay Sci 189:105542

Bian X, Cui YJ, Li XZ (2019) Voids effect on the swelling behaviour of compacted bentonite. Géotechnique 69(7):593–605

Cerfontaine B (2014) The cyclic behaviour of sand, from the Prevost model to offshore geotechnics. PhD Thesis, University of Liege

Cerfontaine B, Dieudonné AC, Radu JP, Collin F, Charlier R (2015) 3D zero-thickness coupled interface finite element: formulation and application. Comput Geotech 69:124–140

Collin F, Li XL, Radu JP, Charlier R (2002) Thermo-hydro-mechanical coupling in clay barriers. Eng Geol 64(2–3):179–193

Cui YJ (2017) On the hydro-mechanical behaviour of MX80 bentonite-based materials. J Rock Mech Geotech Eng 9(3):565–574

Daniels KA, Harrington JF, Sellin P, Norris S (2021) Closing repository void spaces using bentonite: does heat make a difference? Appl Clay Sci 210:106124

Delage P, Marcial D, Cui YJ, Ruiz X (2006) Ageing effects in a compacted bentonite: a microstructure approach. Géotechnique 56(5):291–304

Della Vecchia G, Dieudonné AC, Jommi C, Charlier R (2015) Accounting for evolving pore size distribution in water retention models for compacted clays. Int J Numer Anal Method Geomech 39(7):702–723

Della Vecchia G, Musso G (2016) Some remarks on single- and double-porosity modeling of coupled chemo-hydro-mechanical processes in clays. Soils Found 56(5) 779–789. https://doi.org/10.1016/j.sandf.2016.08.004

Dieudonné AC, Levasseur S, Charlier R, Della Vecchia G, Jommi C (2013) A water retention model for compacted clayey soils. In 3rd International Symposium on Computational Geomechanics (ComGeo III). IC^{2}E, Rhodes, Greece

Dieudonne AC, Della Vecchia G, Charlier R (2017) Water retention model for compacted bentonites. Can Geotech J 54(7):915–925

Dieudonné AC, Gatabin C, Dridi W, Talandier J, Collin F, Charlier R (2023) Heterogeneous swelling of an isotropically compacted bentonite-based material: experimental observations and modelling. Rock Mech Rock Eng. https://doi.org/10.1007/s00603-023-03476-z

Dueck A, Nilsson U (2010) Thermo-hydro-mechanical properties of MX-80. Results from advanced laboratory tests Technical report, SKB

Gatabin C, Talandier J, Collin F, Charlier R, Dieudonné AC (2016) Competing effects of volume change and water uptake on the water retention behaviour of a compacted MX-80 bentonite/sand mixture. Appl Clay Sci 121:57–62

Gens A, Alonso EE (1992) A framework for the behaviour of unsaturated expansive clays. Canadian Geotechnical Journa, 29(6):1013–1032

Gramegna L, Collin F, Talandier J, Imbert C, Charlier R (2020) Hydro-mechanical behaviour of a pellets based bentonite seal: Numerical modelling of lab scale experiments. In E3S Web of Conferences (Vol. 195, p. 04009). EDP Sciences

Gramegna L, Bernachy-Barbe F, Collin F, Talandier J, Charlier R (2022) Pore size distribution evolution in pellets based bentonite hydration: Comparison between experimental and numerical results. Eng Geol 304:106700

Gramegna L, Villar MV, Collin F, Talandier J, Charlier R (2023a) Friction influence on constant volume saturation of bentonite

mixed pellet-block samples, a numerical analysis. Appl Clay Sci 234:106846
Gramegna L, Charlier R, Della Vecchia G (2023b) Numerical study on bentonite permeability evolution upon water hydration. In National conference of the researchers of geotechnical engineering (pp. 319–326). Cham: Springer Nature Switzerland
Gramegna (2021) Hydromechanical behaviour of bentonite sealings in the context of nuclear waste disposals: contributions for engineered barriers evaluation. PhD Thesis, University of Liege.
Guerra AM, Mokni N, Delage P, Cui YJ, Tang AM, Aimedieu P, Bornert M (2017) In-depth characterisation of a mixture composed of powder/pellets MX80 bentonite. Appl Clay Sci 135:538–546
Harrington JF, Daniels KA, Wiseall AC, Sellin P (2020) Bentonite homogenisation during the closure of void spaces. Int J Rock Mech Min Sci 136:104535
Imbert C, Villar MV (2006) Hydro-mechanical response of a bentonite pellets/powder mixture upon infiltration. Applied Clay Science 32(3-4):197–209
Labalette T, Harman A, Dupuis MC, Ouzounian G (2013) CIGEO, the French geological repository project. Atw Internationale Zeitschrift Fuer Kernenergie 58(8–9):499–501
Li X, Zhang G (2015) Minimum penalty for constrained evolutionary optimization. Comput Optim Appl 60:513–544
Martin PL, Barcala JM, Huertas F (2006) Large-scale and long-term coupled thermo-hydro-mechanic experiments with bentonite: the FEBEX mock-up test. J Iber Geol 32(2):259–282
Mokni N, Barnichon JD, Dick P, Nguyen TS (2016) Effect of technological macro voids on the performance of compacted bentonite/sand seals for deep geological repositories. Int J Rock Mech Min Sci 88:87–97
Musso G, Romero E, Della Vecchia (2013). Double-structure effects on the chemo-hydro-mechanical behaviour of a compacted active clay. Geotechnique 63(3):206–220
Navarro V, Asensio L, Gharbieh H, De la Morena G, Pulkkanen VM (2020) A triple porosity hydro-mechanical model for MX-80 bentonite pellet mixtures. Eng Geol 265:105311
Pusch R (1979) Highly compacted sodium bentonite for isolating rock-deposited radioactive waste products. Nucl Technol 45(2):153–157
Romero E (2013) A microstructural insight into compacted clayey soils and their hydraulic properties. Eng Geol 165:3–19
Romero E, Della Vecchia G, Jommi C (2011) An insight into the water retention properties of compacted clayey soils. Géotechnique 61(4):313–328
Saba S, Barnichon JD, Cui YJ, Tang AM, Delage P (2014) Microstructure and anisotropic swelling behaviour of compacted bentonite/sand mixture. J Rock Mech Geotech Eng 6(2):126–132
Seiphoori A, Ferrari A, Laloui L (2014) Water retention behaviour and microstructural evolution of MX-80 bentonite during wetting and drying cycles. Géotechnique 64(9):721–734
Sellin P, Leupin OX (2013) The use of clay as an engineered barrier in radioactive-waste management–a review. Clays Clay Miner 61(6):477–498
Tang AM, Cui YJ, Barnel N (2008) Thermo-mechanical behaviour of a compacted swelling clay. Géotechnique 58(1):45–54
Toprak E, Olivella S, Pintado X (2017) Coupled THM modelling of engineered barriers for the final disposal of spent nuclear fuel isolation. Geol Soc Lond Spec Publ 443(1):235–251
Villar MV (2004) MX-80 bentonite. Thermo-hydro-mechanical characterization performed at CIEMAT in the context of the Prototype Project. Technical report, CIEMAT
Villar MV, Lloret A (2008) Influence of dry density and water content on the swelling of a compacted bentonite. Appl Clay Sci 39(1–2):38–49
Villar MV, Gutiérrez-Alvarez C, Campos G (2023) Bentonite swelling into a void under suction or water flow. Acta Geotech 18(3):1495–1513
Vinsot A, Mettler S, Wechner S (2008) In situ characterization of the Callovo-Oxfordian pore water composition. Phys Chem Earth Parts a/b/c 33:S75–S86
Wang Q (2012) Hydro-mechanical behaviour of bentonite-based materials used for high level radioactive waste disposal. Ph.D. thesis, Université Paris-Est
Wang Q, Tang AM, Cui YJ, Delage P, Barnichon JD, Ye WM (2013) The effects of technological voids on the hydro-mechanical behaviour of compacted bentonite–sand mixture. Soils Found 53(2):232–245
Wang Q, Meng Y, Su W, Ye W, Chen Y (2021) Cracking and sealing behavior of the compacted bentonite upon technological voids filling. Eng Geol 292:106244
Watanabe Y, Yokoyama S (2021) Self-sealing behavior of compacted bentonite–sand mixtures containing technological voids. Geomech Energy Environ 25:100213
Zeng Z, Cui YJ, Conil N, Talandier J (2022) Effects of technological voids and hydration time on the hydro-mechanical behaviour of compacted bentonite/claystone mixture. Géotechnique 72(1):34–47